

# New perspectives of Hall effects from first principles calculations

ShengNan Zhang<sup>1</sup>, Hanqi Pi<sup>1,2</sup>, Zhong Fang<sup>1,2,3</sup>, Hongming Weng<sup>1,2,3</sup>,\* and QuanSheng Wu<sup>1,2†</sup>

<sup>1</sup>*Beijing National Laboratory for Condensed Matter Physics and Institute of physics,  
Chinese academy of sciences, Beijing 100190, China*

<sup>2</sup>*University of Chinese academy of sciences, Beijing 100049, China and*

<sup>3</sup>*Songshan Lake Materials Laboratory, Dongguan, Guangdong 523808, China*

(Dated: January 30, 2024)

The Hall effect has been a fascinating topic ever since its discovery, resulting in exploration of entire family of this intriguing phenomena. As the field of topology develops and novel materials emerge endlessly over the past few decades, researchers have been passionately debating the origins of various Hall effects. Differentiating between the ordinary Hall effect and extraordinary transport properties, like the anomalous Hall effect, can be quite challenging, especially in high-conductivity materials, including those with topological origins. In this study, we conduct a systematic and comprehensive analysis of Hall effects by combining the semiclassical Boltzmann transport theory with first principles calculations within the relaxation time approximation. We first highlight some striking similarities between the ordinary Hall effect and certain anomalous Hall effects, such as nonlinear dependency on magnetic field and potential sign reversal of the Hall resistivity. We then demonstrate that the Hall resistivity can be scaled with temperature and magnetic field as well, analogue to the Kohler's rule which scales the longitudinal resistivity under the relaxation time approximation. We then apply this Kohler's rule for Hall resistivity to two representative materials: ZrSiS and PtTe<sub>2</sub> with reasonable agreement with experimental measurement. Moreover, our methodology has been proven to be applicable to the planar Hall effects of bismuth, of perfect agreements with experimental observations. Our research on the scaling behavior of Hall resistivity addresses a significant gap in this field and provides a comprehensive framework for a deeper understanding of the Hall resistance family, and thus has potential to propel the field forward and spark further investigations into the fascinating world of Hall effects.

## INTRODUCTION

The Hall effect, ever since its discovery by Edwin H. Hall in 1879 [1], has remained one of the most fundamental and notable phenomena, consistently inspiring new research. Its counter part, the anomalous Hall effect (AHE) which followed soon after, showed magnitudes ten times larger in ferromagnetic iron than in nonmagnetic conductors [2]. The AHE phenomenon remained elusive for a century, because it is deeply rooted in advanced concepts of topology and geometry that have been formulated only in recent times [3]. Consequently, topology has revitalized the field of transport, exhibited a series of new phenomena, like quantum Hall effect [4], spin Hall effect [5, 6], anomalous Hall effect [2, 3], planar Hall effect [7–9], negative magnetoresistance [10], chiral anomaly [11, 12] and many others, which are regarded as indicators of new physics.

The AHE phenomenon was first noted in ferromagnetic materials but later was found in nonmagnetic topologically nontrivial materials as well. Given that ordinary and anomalous Hall effect always occur together with similar shape of the resistivity curves and close order of magnitude, especially in high field limit, it is very difficult to distinguish them from each other. For anomalous Hall resistivity(conductivity), scientist usually examine its dependence on longitudinal resistivity(conductivity) to parse it [3], since it could be classified as either intrinsic [13–16] or extrinsic depending on its origin. How-

ever, for ordinary Hall effect, there is seldom study on its scaling behaviors to carry out. In other words, there are relatively clear ways to identify the AHE of Ferromagnetic and topological materials. But it is a challenge to distinguish the resistivity curve with nonlinear and/or sign reversal features of non-ferromagnetic materials from that of AHE. To clarify this, understanding the Hall effect that caused by the Lorentz force and contributions from Berry curvature [17–19] becomes imperative, and further serves as a systematic method to study the Hall effect.

Another captivating phenomenon is the planar Hall effect (PHE). Characterized by an oscillating transverse voltage upon rotating the magnetic field in the plane determined by the current and Hall bar setup surface, the PHE has generated attention across both topologically trivial and nontrivial materials. Initially, the PHE was identified in ferromagnetic materials like GaMnAs, Fe<sub>3</sub>Si, and Fe<sub>3</sub>O<sub>4</sub>, attributed to anisotropic magnetoresistance resulting from significant spin-orbit coupling with magnetic order [9, 20, 21]. However, recent studies have detected PHE in new-found topological insulators and Weyl semimetals, such as Na<sub>3</sub>Bi[22], ZrTe<sub>5</sub> [23], GdPtBi[24, 25], Bi<sub>2-x</sub>Sb<sub>x</sub>Te<sub>3</sub>[26], Cd<sub>3</sub>As<sub>2</sub> [27], ZrTe<sub>5- $\delta$</sub>  [28], WTe<sub>2</sub> [29], SmB<sub>6</sub>[30], Te [31], and Sr<sub>3</sub>SnO [32]. There are various proposed mechanisms behind PHE including anisotropic Fermi surfaces, time-reversal symmetry breaking in topological surface states, and the chiral anomaly in Weyl semimetals. Wang et al. further enriched this understanding by shedding light on the orbital

contribution to PHE, pointing out that traditional theories might overlook this aspect [33]. It is also noteworthy to mention that the generated in-plane transverse Hall voltage can be classified as either the Planar Hall Effect or the in-plane Hall effect, depending on the even or odd function of the magnetic field [33, 34]. These fresh insights into the field of Hall effects suggest that there's still much to uncover and explore. Moreover, the advantages of PHE sensors include their thermal stability, high sensitivity, and very low detection limits, supporting a wide range of advanced applications such as nano-Tesla magnetometers, current sensing, and low magnetic moment detection. This makes them promising for applications in the integrated circuits industry.

The temperature dependence of resistivity is always an important and intriguing phenomenon to understand the magneto transport properties of materials. Kohler's rule [35, 36], a magneto resistivity scaling behavior that collapses a series of magnetoresistance curves with different temperatures onto a single curve, has long been established and studied. Recently, researchers reported a transformative "turn-on" phenomenon within the resistivity-temperature curve  $\rho(T)$ , a unique feature of materials with extremely large magnetoresistance [37–45]. This phenomenon was once considered as a magnetic-field-driven metal-insulator transition, but perfectly reproduced and explained by Kohler's rule, as demonstrated by the work of Wang and colleagues [38]. The successful application of Kohler's rule to longitudinal resistivity (or MR) raises an intriguing query: Does a scaling law exist for transverse resistivity, such as Hall resistivity? Further exploration and study in this fascinating area of research promise to yield new insights and deepen our understanding of the fundamental principles that govern magnetotransport behavior.

Despite the increasing interest in topological properties and its correlation with transport phenomena, the Hall effect - rooted in semiclassical Boltzmann theory - remains a cornerstone of magnetotransport understanding. Our previous work [46] demonstrates that the Lorentz force and Fermi surface geometry play crucial roles in magnetoresistance. Combining semiclassical Boltzmann theory with first principles calculations has proven powerful in predicting the magnetoresistance of non-magnetic materials, as observed from experiments, such as the non-saturating MR of bismuth, Cu [46], SiP<sub>2</sub> [47],  $\alpha$ -WP<sub>2</sub> [48], MoO<sub>2</sub> [49], TaSe<sub>3</sub> [50], ReO<sub>3</sub> [51], and large anisotropic MR of type-II Weyl semimetal WP<sub>2</sub> [46], ZrSiS [52] et al. Yet, it is evident that comprehensive and systematic studies into Hall effect aspect are notably lacking, especially from first principles calculation studies. Addressing this gap in knowledge is crucial to fully comprehend the various manifestations of the Hall effect, whether in topologically trivial or nontrivial materials.

In this study, we present a comprehensive first princi-

ples exploration of the Hall effect, encompassing both the ordinary and planar Hall effects, to complete the story of magnetoresistance within the context of Boltzmann transport theory and relaxation time approximation in our previous work [46]. First we notice the Hall resistivity of some nonmagnetic materials, e.g., PtTe<sub>2</sub> and ZrSiS, show some distinct features similar to those of ferromagnetic ones, such as the nonlinear slope. Accordingly, we construct multi-band toy models to simulate their Hall resistivity, and illustrate that the intricate shape of Hall resistivity curve is determined by the interplay between mobility and concentration of charge carriers. For instance, materials with multi type charge carrier exhibit nonlinear and/or sign reversal Hall resistivity, a characteristic resemble the AHE in ferromagnetic metals [17, 19] and in the topological insulator ZrTe<sub>5</sub> [53]. We then take a typical two-band material PtTe<sub>2</sub> to demonstrate these features, similar to the AHE, could be calculated and interpreted in the scope of the Boltzmann transport theory, resulting in surprisingly good agreement with experiment measurements.

Furthermore, we found there exists a scaling rule to depict the temperature effect on the Hall resistivity, analogue to the Kohler's rule of magnetoresistance. Consequently, we name it as Kohler's rule of Hall resistivity. To demonstrate this, we chose PtTe<sub>2</sub> and ZrSiS as representative materials to elucidate the scaling behavior of their Hall resistivity relying on the magnetic field and temperature. Our theoretical calculations agree well with the corresponding experimental results, underscoring the veracity of this semiclassical approach. To our knowledge, Kohler's rule of Hall resistivity has never been made explicitly, but it is extremely important to help understanding the Hall resistivity scaling of multi type charge carrier materials.

Ultimately, we successfully describe and explain the Planar Hall effect in bismuth within this framework of semiclassical Boltzmann transport theory. In all, our study provides a methodology for systematically accounting transverse resistivity from semiclassical Boltzmann transport over a wide range, encompassing nonlinear properties, scaling behaviors, and Planar Hall resistivity originating from Fermi surface geometry. Moreover, the Chambers equation, as the spirit of the semiclassical magnetotransport theory, always lies at the heart of the calculation of various resistivity.

Our paper is organized as follows. In Section II, we review our computational methodology. Section III considers a few multi-band models to specify the nonlinear features of Hall resistivity and apply it to real material PtTe<sub>2</sub>. Section IV discusses the scaling behavior of Hall resistivity concerning temperature in PtTe<sub>2</sub> and ZrSiS materials. Section V focuses on the planar Hall effect. Finally, Section VI summarizes our work.

## METHODOLOGY

In this work, we employ a sophisticated methodology combining first principles calculations and semiclassical Boltzmann transport theory to accurately compute magnetoresistance and Hall effects in models and real materials, ZrSiS, PtTe<sub>2</sub> and bismuth. First we construct tight-binding models using the first principles calculation software such as VASP [54, 55] along with Wannier function techniques such as Wannier90 [56]. This approach allows us to obtain Fermi surfaces consistent with first principles calculation results, providing an accurate representation of the electronic structure of the materials under study.

After constructing tight-binding models, we apply the Chambers equation for rigorous treatment of the Lorentz force generated by the magnetic field acting on electrons within the Fermi surface. By precisely solving the semiclassical Boltzmann equation in the presence of a magnetic field, we get the conductivity for each energy band  $\sigma_n(B)$  in the investigated materials. The resistivity is obtained by inverting the total conductivity tensor, which is derived by summing the conductivities across all energy bands  $\sigma(B) = \sum_n \sigma_n(B)$ . Our detailed computational methods are thoroughly explained in Reference [46, 57] and implemented within the WannierTools software package [58].

Furthermore, we construct and analyze tight-binding toy models to explore the underlying physics governing magnetoresistance and Hall effects. The development and implementation of these toy models, as well as the results obtained, are extensively described in the Supplemental Material ([59]). This comprehensive methodology enables a deeper understanding of the complex interplay between electronic structure, magnetic fields, and transport properties in a broad of materials.

## MULTI-BAND MODEL

In the early stages of Hall effect research, it was generally considered that the Hall resistivity  $\rho_{yx}$ , exhibits a linear relationship with the magnetic field  $B_z$ , as predicted by the Lorentz force acting on single charge carriers. Interestingly, the Hall resistivity exhibits nonlinear slope when there are both electron and hole charge carriers, even without complex Fermi surface structure, which are already reproduced in previous works [46, 60]. Consequently, examining the interplay between multiple types of charge carriers would serve as foundations to understand various Hall resistivity features in real materials.

On the other hand, regarding the similarity and perplexity features of the ordinary and anomalous Hall resistivity [53], a comprehensive analysis is essential to clarify these ambiguity and draw a global picture. Therefore in this section, we construct several isotropic multi-band toy

models to simulate Hall resistivity with typical behaviors, including nonlinearity, sign reversal (s-shaped near the origin), and plateaus.

We begin with the isotropic two-band model, which involves four parameters:  $n_e$  and  $n_h$  representing the densities of electron and hole charge carriers, and  $\mu_e$  and  $\mu_h$  denoting the mobilities of electrons and holes, respectively. The longitudinal and transverse resistivities for this model are given by the following expressions:

$$\begin{aligned}\rho_{xx} &= \frac{1}{e} \frac{(n_e\mu_e + n_h\mu_h) + (n_e\mu_h + n_h\mu_e)\mu_e\mu_h B^2}{(n_e\mu_e + n_h\mu_h)^2 + (n_h - n_e)^2\mu_e^2\mu_h^2 B^2} \\ \rho_{yx} &= \frac{B}{e} \frac{(n_h\mu_h^2 - n_e\mu_e^2) + (n_h - n_e)\mu_e^2\mu_h^2 B^2}{(n_e\mu_e + n_h\mu_h)^2 + (n_h - n_e)^2\mu_e^2\mu_h^2 B^2}\end{aligned}\quad (1)$$

where we take the convention such that the positive value of  $\rho_{yx}(B \rightarrow \infty)$  indicates net hole concentration as  $n_h > n_e$ .

Despite its apparent simplicity, this model is able to reproduce results that closely agree with experiment. It is frequently employed to fit MR and Hall resistivity in experiments, enabling the determination of charge carrier concentration and mobility of real materials. It is noteworthy that identical results can be achieved if one utilizes first principles calculations combined with the Boltzmann transport method to simulate isotropic multi-band model [59].

The competition between constant and magnetic field dependent terms in Eq. (1) suggest that  $\rho_{xx}$  and  $\rho_{yx}$  may exhibit distinct behaviors under extremely low and high magnetic fields. Meanwhile, the interplay between different charge carriers, i.e., concentration and mobility, would change the concrete form of the Hall resistivity curves. We initiate our analysis of Eq. (1) by examining the most simple case where one type of charge carrier dominates the transport, characterized by  $\left| \frac{n_h - n_e}{n_h + n_e} \right| \sim 1$  (assuming  $n_h \gg n_e$ ). In the high magnetic field limit, the longitudinal resistivity is reduced to  $\rho_{xx} = \frac{1}{en_h\mu_h}$ , which saturates to a constant value. While, the Hall resistivity  $\rho_{yx} = \frac{B}{en_h}$  exhibits a linear dependence on the magnetic field. This extreme case provides an perfect description for most simple metals, such as alkali metals (except potassium), and to a lesser extent for noble metals.

Then we consider the case of two types of charge carriers that perfectly compensated with each other, i.e.,  $n_e = n_h$  and  $\left| \frac{n_h - n_e}{n_h + n_e} \right| = 0$ . The resistivity reduces to

$$\rho_{xx} = \frac{(n_e\mu_e + n_h\mu_h) + (n_e\mu_h + n_h\mu_e)\mu_e\mu_h B^2}{e(n_e\mu_e + n_h\mu_h)^2} \quad (2)$$

$$\rho_{yx} = \frac{(n_h\mu_h^2 - n_e\mu_e^2)B}{e(n_e\mu_e + n_h\mu_h)^2} \quad (3)$$

Clearly, the longitudinal resistivity  $\rho_{xx}$  scales quadratically with the magnetic field, while the Hall resistivity  $\rho_{yx}$  exhibits a linear dependence on the magnetic field. This model is capable of explaining a significant portion

TABLE I: The field dependence of magnetic resistivity of non-magnetic metal/semimetals in the low-field and high-field limits.

type of compensation	magnetic field (B)	magneto-resistivity $\rho_{xx}$	Hall resistivity $\rho_{yx}$
$\frac{ n_h - n_e }{ n_h + n_e } \rightarrow 0$ (almost compensated)	$\omega_c \tau \rightarrow 0$ (low)	$\rho_0 + A\rho_0\mu_e\mu_h B^2$ <sup>[1]</sup>	$\frac{B(n_h\mu_h^2 - n_e\mu_e^2)}{e(n_e\mu_e + n_h\mu_h)^2}$
	$\omega_c \tau \gg 1$ (high)	$\rho_{st.}$ <sup>[3]</sup>	$\frac{B}{e(n_h - n_e)}$
$n_e = n_e$ but $\mu_e \neq \mu_h$ (Fully compensated)	$\omega_c \tau \rightarrow 0$ (low)	$\rho_0 + A\rho_0\mu_e\mu_h B^2$ <sup>[1]</sup>	$\frac{B(n_h\mu_h^2 - n_e\mu_e^2)}{e(n_e\mu_e + n_h\mu_h)^2}$
	$\omega_c \tau \gg 1$ (high)		$\frac{B(n_h\mu_h^2 - n_e\mu_e^2)}{e(n_e\mu_e + n_h\mu_h)^2}$
$\frac{ n_h - n_e }{ n_h + n_e } \rightarrow 1$ (one carrier dominated)	$\omega_c \tau \rightarrow 0$ (low)	$\rho_0$ <sup>[2]</sup>	$\frac{B(n_h\mu_h^2 - n_e\mu_e^2)}{e(n_e\mu_e + n_h\mu_h)^2}$
	$\omega_c \tau \gg 1$ (high)	$\rho_{st.}$ <sup>[3]</sup>	$\frac{B}{e(n_h - n_e)}$

$$^1 A = \frac{(n_e\mu_e + n_h\mu_h)}{(n_e\mu_e + n_h\mu_h)}.$$

$$^2 \rho_0 = \frac{1}{e(n_e\mu_e + n_h\mu_h)}$$
 is the zero-field longitudinal resistivity.

$$^3 \rho_{st.} = \frac{n_e\mu_e + n_h\mu_h}{e(n_h - n_e)^2\mu_e\mu_h}$$
 is the saturated longitudinal resistivity at high-field limit.

\* When both carriers have the same temperature dependent relaxation time  $\tau$ ,  $\rho_0 \propto 1/\tau$ ,  $A = const.$ ,  $\rho_{st.} \propto \rho_0 \propto 1/\tau$

of extremely large magnetoresistance observed in both topological trivial and non-trivial materials. Given the fact that most materials deviate somewhat from perfect compensation, the longitudinal and Hall resistivity both depart from the ideal shape and exhibit sub-quadratic and non-linear behavior accordingly [47, 61].

As the situation becomes more complex, i.e., the charge carriers deviates slightly from perfect compensation, but remains close with each other as  $n_h \sim n_e$ . The behaviors of Hall resistivity show intricacy, since it sensitively depends on the competition between the charge carriers through their concentration, mobility, and magnetic field strength. At low magnetic fields ( $B \rightarrow 0$ ), the constant terms in the denominators dominate and hence the term  $(n_h - n_e)^2\mu_e^2\mu_h^2 B^2$  can be safely disregarded. This results in the expression  $\rho_{xx}(B \rightarrow 0) \propto \frac{\mu_e\mu_h B^2}{e(n_e\mu_e + n_h\mu_h)}$ , still exhibiting a parabolic dependence on the magnetic field. The Hall resistivity  $\rho_{xy}$  is given by  $\frac{(n_h\mu_h^2 - n_e\mu_e^2)}{e(n_e\mu_e + n_h\mu_h)^2} B$ , which is proportional to  $B$ , and the sign of slope of the Hall curve depends on  $(n_h\mu_h^2 - n_e\mu_e^2)$ . At very high magnetic fields ( $B \rightarrow \infty$ ), the terms with  $B^2$  in the numerator and denominator of  $\rho_{xx}$  cancel each other out, leading to a saturation of longitudinal resistivity. The Hall resistivity still scales linearly as  $\rho_{xy} \propto \frac{B}{e(n_h - n_e)}$ , but the sign of slope now depends on  $(n_h - n_e)$ , which is distinct from the low-field case. Accordingly, the Hall resistivity curve may possess completely opposite slopes in the low and high magnetic field limits, generating various curve shapes. For convenience, we summarize the results of our two-band model in Table I.

Next, we shall present two examples to gain specific insights into various features of Hall resistivity originating from the interplay between different charge carriers. Consider two types of charge carriers with the following concentration and mobility values:  $n_e = 1$ ,  $\mu_e = 4$ ,  $n_h = 1.2$ , and  $\mu_h = 1$ . In this case, we have  $n_e < n_h$ ,  $\mu_e > \mu_h$ , and  $n_e\mu_e^2 > n_h\mu_h^2$ , which is expected to result in distinct Hall resistivity slopes under low and high magnetic field. We

plot the longitudinal and Hall resistivity  $\rho_{xx}, \rho_{yx}$  for this case in Fig. 1. To fully understand their behaviors, it is essential to discuss them on different magnetic field ranges, namely low, moderate, and high magnetic fields. When we consider a large magnetic field scale (up to 120), we observe that the Hall resistivity (red line) shows a linear dependence on the magnetic field, while the longitudinal resistivity (blue line) saturates quickly (Fig. 1(a)). This is a common observation for semimetals or semiconductors, precisely in line with our intuition. However, this is not the integrity physical picture. When enlarging the magnetic field axis, we discover entirely different behaviors in the low and moderate magnetic field regime. This is plotted in the inset of Fig. 1(b) and (c).

Within the low magnetic field ranging from 1 to 3 shown as Fig. 1(c), the longitudinal resistivity  $\rho_{xx}$  (blue line) exhibits a nearly (or sub) parabolic scaling, while the Hall resistivity  $\rho_{xy}$  (red line) shows a sign-reversal feature, as mentioned previously. The slope of the Hall resistivity initially appears positive due to  $(n_h\mu_h^2 - n_e\mu_e^2) > 0$  at low magnetic field, and then changes to negative as the magnetic field increases, determined by  $n_h - n_e < 0$ . When observing the resistivity curve at a moderate magnetic field scale, e.g., 0 to 5, as depicted in Fig. 1(b), the sign-reversal feature becomes less distinct but appears similar to the anomalous Hall effect (indicated by the black dashed line and the area between it and the red curve). This moderate magnetic field range is the most frequently used in experiments measurement.

To apply these analysis to real two-band materials, we choose a representative of type-II Dirac semimetal PtTe<sub>2</sub>. Pavlosiuk and Kaczorowski [61] have performed magnetic transport measurement on PtTe<sub>2</sub> and reported that the longitudinal resistivity depends on magnetic field of the power law  $\rho_{xx} \propto B^{1.69}$ , and that the Hall effect data exhibits a multi-band character with moderate charge carrier compensation. Both of these behaviors indicate its charge carriers deviate from perfect compensation. We reproduce these feature in our calculations, and plot both

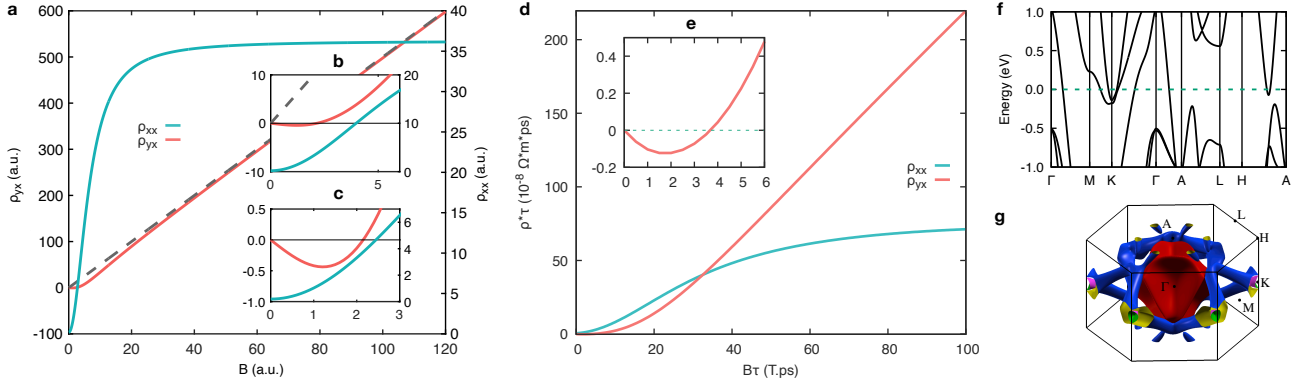


FIG. 1: Longitudinal  $\rho_{xx}$  (cyan line) and Hall resistivity  $\rho_{yx}$  (red line) of (a) a 2-band model and (d) a material PtTe<sub>2</sub>. (a) Parameters for the 2-band model are  $n_e = 1, n_h = 1.2, \mu_e = 4, \mu_h = 1$  satisfying the conditions  $n_e < n_h, \mu_e > \mu_h, n_h \mu_h^2 < n_e \mu_e^2$ . The grey dashed lines visible in (a) represent the Hall resistivity in the scenario of a high-limit magnetic field. Insets (b) (c) and (e) are enlarged views of the main panel, each within a different magnetic field range. Please note for (a)-(c), the left and right vertical axis are corresponding to  $\rho_{yx}$  and  $\rho_{xx}$  respectively. (f) (g) the energy band structures and Fermi surfaces of PtTe<sub>2</sub> respectively.

longitudinal and Hall resistivity curves in Fig. 1(d). The band structure of PtTe<sub>2</sub>, shown in Fig. 1(f), exhibits complex structure near the Fermi energy and hence intricate Fermi surface displayed in Fig. 1(g). This is consistent with the quantum oscillation results in Ref. [61], which confirm more than three electron and hole pockets but only one electron and one hole bands dominating the transport near Fermi level.

Now we shall compare our calculated results with the experimental measurements reported in Ref [61]. The measured MR exhibits a sub-quadratic power law dependence on magnetic field and remains unsaturated until  $B = 8$  T (Fig.2a in Ref [61]). In our calculations, the blue line of longitudinal resistivity  $\rho_{xx}$  in Fig. 1(d) also shows sub-quadratic dependence on magnetic field under  $B\tau$  no more than 10 T.ps but becomes saturated at very large field over  $B\tau = 50$  T.ps. On the other hand, the Hall resistivity  $\rho_{yx}$  exhibits a complex manner: at low temperature  $T = 2 \sim 25$  K (Fig.6a in Ref [61]), i.e., it starts as negative, drop to a minimum, then switches to positive, and continues to rise with increasing magnetic field. Our calculated results perfectly reproduce the sign reversal feature, as shown in Fig. 1(e): the negative minimum of Hall resistivity appears around  $B\tau = 2$  T.ps, and then changes to positive around  $B\tau = 4$  T.ps, which agrees quite well with experimental measurements.

Furthermore, we go deeper to a three-band model, for example one type of electron charge carrier and two types of hole charge carriers. By explicitly writing their resistivity equations at low magnetic field ( $B \rightarrow 0$ ) explicitly (see the detailed equations A.16-A.17 in [59]), we can see that the sign of the Hall resistivity is determined by the term  $-n_e \mu_e^2 + n_{h1} \mu_{h1}^2 + n_{h2} \mu_{h2}^2$ , owing to the interplay of both concentration and mobility of multiple charge carriers. Regarding the high magnetic fields case ( $B \rightarrow \infty$ ), the resistivity is written as,

$$\rho_{xx} = \frac{n_{h1} \mu_e \mu_{h2} + n_{h2} \mu_e \mu_{h2} + n_e \mu_{h1} \mu_{h2}}{e(-n_e + n_{h1} + n_{h2}) \mu_e \mu_{h1} \mu_{h2}}$$

$$\rho_{yx} = \frac{B}{e(-n_e + n_{h1} + n_{h2})} \quad (4)$$

which is evident that the sign of Hall resistivity is only determined by the net concentration of multiple charge carriers  $-n_e + n_{h1} + n_{h2}$ , implying that the net charge quantity dictates the slope of Hall resistivity under high magnetic fields. Based on the distinct form of Hall resistivity under low (see equation A.16-A.17 in [59]) and high magnetic fields (Eq.4), it is natural to conclude that the Hall resistivity may change sign when altering the magnitude of magnetic field.

The physical origin of this sign reversal is the competition between different type of charge carriers. We could understand it qualitatively as follows. Through the previous analysis, the Hall resistivity finally shows the expected sign at high field limit, i.e., the net charge concentration. However, at low magnetic field it sensitively depends on practical motion trajectory. We take the standard definition of a dimensionless quantity  $\omega\tau = \frac{e}{m} B\tau$  to mark achievement of the cyclotron motion, from which one finds that charge carriers with larger masses will complete one circle more slowly than the lighter one. Consequently, the lighter charge carrier exhibits their charge onto the sign of Hall curve earlier than the heavier ones. As all charge carriers have completed numerous circles under high magnetic field, the net quantity of charge carriers takes over to determine the sign of Hall resistivity. If the Hall resistivity signs differ in low and high magnetic field scenarios, then a sign reversal must occur.

We shall present two examples to illustrate how the Hall resistivity sensitively depends on the details of the charge carriers, as shown in Fig. 2. From the three-band

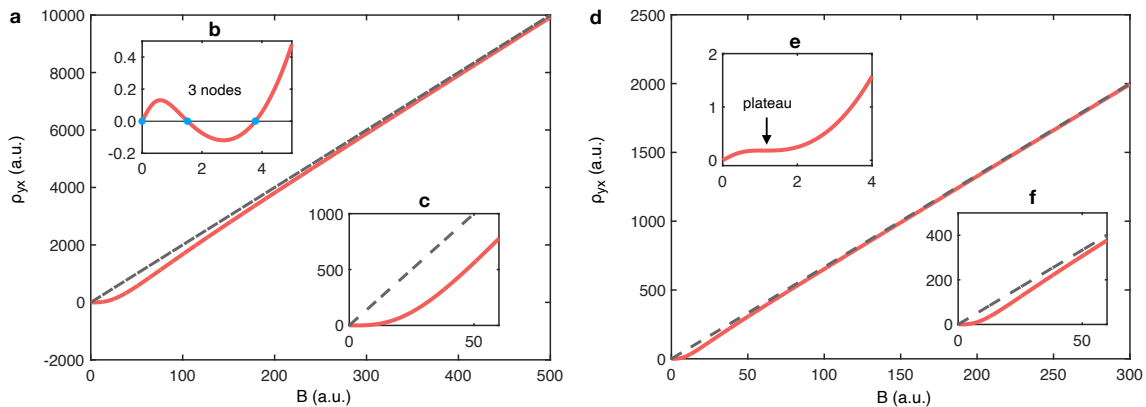


FIG. 2: Hall resistivity  $\rho_{yx}$  of two 3-band models with parameters  $n_e = 1$ ,  $n_{h1} = 0.5$ ,  $n_{h2} = 0.55$ ,  $\mu_e = 1$ ,  $\mu_{h1} = 0.5$ ,  $\mu_{h2} = 2.5$ ,  $n_{h1} + n_{h2} > n_e$  for (a), exhibiting a 3-node structure, and  $n_e = 1$ ,  $n_{h1} = 0.5$ ,  $n_{h2} = 0.55$ ,  $\mu_e = 1$ ,  $\mu_{h1} = 0.65$ ,  $\mu_{h2} = 2.5$  for (d), exhibiting a plateau structure. Insets (b) (c) and (e) (f) are enlarged views of the main panel. The grey dashed lines represent the Hall resistivity in the scenario of a high-limit magnetic field.

model, one can easily determine the slope of the Hall resistivity at very low and high magnetic fields, but not in between. Here, we consider two cases that both satisfy  $-n_e\mu_e^2 + n_{h1}\mu_{h1}^2 + n_{h2}\mu_{h2}^2 > 0$  and  $-n_e + n_{h1} + n_{h2} > 0$ . As shown in Fig. 2(a) and (d), the Hall resistivity is plotted with a large magnetic field scale view, and both cases exhibit roughly positive Hall resistivity. First, let's consider the concentration and mobility of charge carriers with  $n_e = 1$ ,  $\mu_e = 1$ ,  $n_{h1} = 0.5$ ,  $\mu_{h1} = 1$ , and  $n_{h2} = 0.55$ ,  $\mu_{h2} = 2.5$ . In Fig. 2(b), the Hall resistivity initially shows a positive slope, but soon changes to negative and then back to positive again, resulting in sign reversal and 3-node oscillation features at low magnetic field regime. However, if we plot the Hall resistivity within the intermediate magnetic field range, a feature resembling the anomalous Hall effect occurs around the origin, as shown in Fig. 2(c). As a comparison case shown in Fig. 2(d), we only modify the mobility of one type of hole charge carriers from  $\mu_{h1} = 0.5$  to  $\mu_{h1} = 0.65$ , while keeping other parameter unchanged. This still satisfies the condition that the slopes of Hall resistivity is positive under very low and high magnetic fields. However, instead of a 3-node oscillation feature, a plateau appears in the Hall resistivity, as shown in Fig. 2(e). This can be understood by calculating the derivative of the Hall resistivity  $\frac{d\rho_{yx}}{dB}$ . Whether  $\frac{d\rho_{yx}}{dB} = 0$  occurs once or twice determines the presence of a plateau or 3-node oscillation features, respectively. In all, we observe that ordinary Hall resistivity curve can appear features similar to the AHE ones, i.e., nonlinear slope and sign reversal, only considering semiclassical Boltzmann transport approach with multi types of charge carriers under intermediate magnetic field regime.

### THE HALL RESISTIVITY SCALING BEHAVIOR AND TEMPERATURE EFFECT

Kohler's rule is a particularly common phenomenon when one studies the scaling behaviors of MR, which states that the MR should be a function of the combined variable  $\frac{B}{\rho_0}$ , expressed as  $\text{MR} = \frac{\Delta\rho}{\rho_0} = F\left(\frac{B}{\rho_0}\right)$ . In principle, assuming that the scattering mechanisms of the material remain unchanged, the conductivity is expected to be proportional to the drift length divided by the relaxation time. As the magnetic field intensifies, the drift length correspondingly decreases, primarily because it is inversely proportional to the magnetic field. [62]. Therefore, the conduction behavior of charge carriers can be scaled down when increasing the magnetic field, i.e., that all MR curves should collapse onto a single curve. This physical scaling picture is consistent with Kohler's rule.

It is not difficult to find that the Chambers equation already embraces Kohler's rule after close and careful study. Chambers equation, represented by Eq. A.1 ([59]), states that the product of resistivity and relaxation time is a function of the combined variable of magnetic field and relaxation time, i.e.,  $\rho\tau = f(B\tau)$ . Recall that the zero-field resistivity is inversely proportional to the relaxation time as  $\rho_0 \propto \frac{1}{\tau}$  in the Drude model, which is taken as a basic hypothesis in this section. Thus we have  $B\tau \sim \frac{B}{\rho_0}$ , and the Chambers equation recovers Kohler's rule. Moreover, the Chambers equation provides a more comprehensive framework for calculating all the elements of resistivity tensor, including the transverse resistivity elements; while Kohler's rule only concerns longitudinal resistivity. Namely, Chambers equation offers a more extensive formulation to investigate the scaling behavior of resistivity tensor.

When the MR curves are scaled according to different temperatures, they collapse onto a single curve for most materials. This implies temperature is another scaling

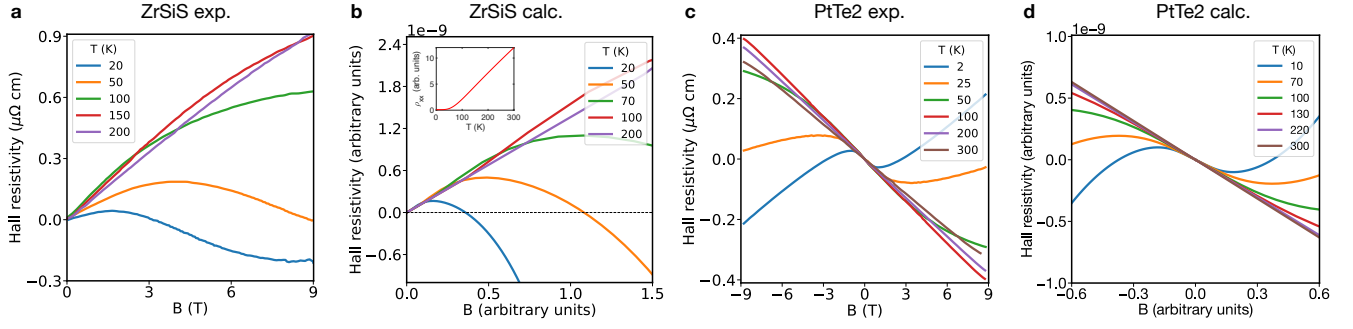


FIG. 3: Field dependence of the Hall resistivity of ZrSiS and PtTe<sub>2</sub>, (a) (c) Measured Hall resistivity at different temperatures for ZrSiS and PtTe<sub>2</sub>, replotted from Ref. [63] and Ref. [61] respectively, (b), (d) Interpretations based on Kohler’s rule, with Hall resistivity numerically calculated at low temperatures for both materials. Inset in (b): Longitudinal resistivity of ZrSiS at B=0 using the Bloch-Grüneisen model.

variables besides magnetic field. The temperature does not exist explicitly in the resistivity expression but hidden in the zero field resistivity  $\rho_0$  or relaxation time  $\tau$ . It’s important to note that temperature impacts not only the relaxation time but also causes a shift in the Fermi energy and modifies the Fermi distribution function, leading to a comprehensive alteration of the transport properties. However, we are concerned with the effect of temperature on relaxation time in this work.

To better understand the scaling behavior of Hall resistivity with temperature, we briefly review the influence of thermal effects on resistivity through the relaxation time. Within the semiclassical transport framework, the relaxation time encompasses all scattering processes and is a key determinant of resistivity, which can be expressed as  $\rho_0 \propto \frac{1}{\tau}$  in the absence of a magnetic field. Different scattering mechanisms lead to various relationships between resistivity and temperature. At very low temperatures, resistivity becomes temperature-independent ( $\rho_0 \propto T^0$ ) due to solid impurity scatterings, which are unaffected by temperature. With increasing temperature, electron-electron (e-e) and electron-phonon (e-h) scatterings begin to dominate.

Typically, e-e scattering contributes to resistivity following  $\rho_0 \propto \frac{1}{\tau} \propto T^2$ . Given that the relaxation time  $\tau$ , originating from e-e scattering in metals at room temperature, is of the order of  $10^{-10}$  seconds—approximately  $10^4$  times larger than that of other scattering mechanisms—its impact on resistivity is relatively minor compared to others. E-h scattering also plays a crucial role in degrading currents, but its temperature dependence is more intricate. At relatively low temperatures (below the Debye temperature  $\Theta_D$ ), the resistivity follows a power law relationship with temperature as  $\rho_0 \propto T^5$ . In contrast, at higher temperatures ( $T > \Theta_D$ ), the resistivity demonstrates a linear temperature dependence, specifically  $\rho_0 \propto T$ .

Indeed, empirical descriptions provide qualitative insights, but for more precise quantitative analysis, we introduce the Bloch-Grüneisen (BG) model [64] in order

to simulate the resistivity of a metallic system at zero magnetic field, which is written as,

$$\rho_0 \equiv \rho(T, B = 0) = \rho(T = 0, B = 0) + A \left( \frac{T}{\Theta_D} \right)^n \int_0^{\Theta_D/T} \frac{t^n}{(e^t - 1)(1 - e^{-t})} dt \quad (5)$$

where,  $\rho(T = 0, B = 0)$  denotes the residual resistivity at zero magnetic field, and  $\Theta_D$  is the Debye temperature. This BG equation effectively characterizes phonon scattering across the full temperature spectrum. In this context, the zero-field resistivity  $\rho(T, B = 0)$  can be approximated by a power law,  $T^n$ , in the low temperature regime (when  $T \ll \Theta_D$ ), and transitions to a linear,  $\sim T$ , dependence in the high-temperature region. Utilizing the BG model allows us to quantitatively calculate the longitudinal resistivity as a function of temperature, considering the realistic scattering processes of materials.

To derive temperature dependent Hall resistivity curves varying with magnetic field from our calculated results  $\rho\tau = f(B\tau)$ , as per the Chambers equation, it is necessary to replace the relaxation time  $\tau$  in the combined variables  $B\tau$  and  $\rho\tau$  with the temperature-dependent zero-field resistivity  $\rho_0$ . This approach is based on the hypothesis that  $\tau \propto \frac{1}{\rho_0}$ , essentially reversing the scaling analogy of Kohler’s rule. The temperature-dependent zero-field resistivity  $\rho_0$  can be computed using the Bloch-Grüneisen (BG) model as shown in Eq. 5 and is depicted in the inset of Fig.3. For simplicity, we assume that each temperature corresponds to a constant relaxation time, ensuring that the scattering mechanism remains unchanged within the relaxation time approximation. Consequently, we compare our calculated Hall resistivity (as illustrated in Fig.3(b)) with the experimental results (shown in Fig.3(a)) for ZrSiS at various temperatures. The comparison reveals a relatively good agreement, capturing most of the essential features.

For example, the Hall resistivity curves display distinct shapes at different temperatures, rather than a uniform pattern. Notably, at relatively low temperatures (up to

$T = 50\text{K}$ ), these curves exhibit a transition from positive to negative values under small magnetic fields. This transition is marked by an intercept on the  $B$ -axis, which indicates a change in the slope of the Hall resistivity. As the temperature increases, the bending of the curves becomes less pronounced. The behavior transitions from a downward trend to a relatively flat response and then eventually to a linear increase with the rising magnetic field.

To further elucidate this point, we take the calculated curves at very low temperatures as a reference, such as  $T = 20\text{K}$ , where the relaxation time is large due to very few scatterings. As temperature increases, the relaxation time decreases, hence the transformation of the horizontal axis from  $(B\tau)$  to  $B$  leads to an increasing intercept of the Hall resistivity curve on the  $B$ -axis. This increasing intercept implies that the positive segment of the Hall resistivity curve gradually occupies a larger proportion of the whole  $B$ -axis range. Along with the relaxation time significant decreasing, ranging from one to several dozen times, it is expected that the negative segment of the Hall resistivity curve will gradually diminish at relatively high temperature as shown in Fig.3(b). Based on this observation, it is suggested that a series of Hall resistivity curves at different temperature of ZrSiS are the result of relaxation time varying with temperature.

In order to further clarify this point, we consider the calculated curves at very low temperatures, such as  $T = 20\text{K}$ , where the relaxation time is large due to minimal scatterings. As the temperature rises, the relaxation time shortens, resulting in increase of intercept of the Hall resistivity curve on the  $B$ -axis due to the horizontal axis transforming from  $(B\tau)$  to  $B$ . This increasing intercept indicates that the positive portion of the Hall resistivity curve gradually becomes more prominent across the entire  $B$ -axis range. With the relaxation time significantly decreasing, by factors ranging from one to several dozen, the negative segment of the Hall resistivity curve is expected to progressively diminish at relatively high temperatures, as demonstrated in Fig.3(b). From this observation, we infer that the series of Hall resistivity curves at different temperatures for ZrSiS are a manifestation of the relaxation time variation with temperature.

Expanding our analysis to additional materials, we compare the experimentally measured Hall resistivity of PtTe<sub>2</sub> with our corresponding calculated results in Fig.3(c) and (d), demonstrating good agreement. By applying the same analytical approach used for ZrSiS, the behavior of Hall resistivity in PtTe<sub>2</sub> as temperature increases becomes readily understandable. Differing from the presentation in Fig.3(a) and (b), in Fig.3(c) and (d), we plot the Hall resistivity against the magnetic field from negative to positive direction, facilitating a direct comparison between our calculations (Fig.3(d)) and experimental data (Fig.3(c)). From lower temperatures ( $T = 2\text{K} \sim 25\text{K}$ ) to higher ones ( $T = 50\text{K} \sim 300\text{K}$ ), the

interception of the Hall resistivity curves on the  $B$ -axis shows a progressive change from minimal to significant, eventually reaching infinity. We do not further detail the characteristic Hall curves of PtTe<sub>2</sub>, as they originate from the same mechanisms observed in ZrSiS, and both sets of data show reasonable agreement with experimental results.

To our knowledge, the scaling behavior of Hall resistivity has been hardly studied both experimentally and theoretically. The reasons may be as follows; the scaling behavior of Hall resistivity is not that straight forward like the Kohler's rule for longitudinal resistivity. On one hand, the Hall resistivity linearly depends on magnetic field of material with single charge carriers for many metals, semimetals and semiconductors. Moreover, the behavior of the Hall resistivity under low and high magnetic field limit remains unaffected by temperature, as shown in Table I, eliminating the need for scaling. On the other hand, in materials with multiple types of charge carriers that compensate each other, such as ZrSiS and PtTe<sub>2</sub>, the Hall resistivity exhibits a complex function of magnetic field and temperature. This complexity often leads to nonlinear and sign reversal features, which are sometimes misinterpreted as Anomalous Hall Effect (AHE) or indicative of new physics. In contrast, longitudinal MR often shows a distinct power law dependence on magnetic field, making the scaling behavior more apparent and easier to summarize.

Additionally, we want to point out that our calculated Hall resistivity deviates from the experimental measurements at low temperatures (such as  $T = 20, 50\text{K}$ ) and high magnetic fields in Fig.3. This deviation suggests that the relaxation time varies not only with temperature but also with other parameters, such as the band index and the momentum  $k$ .

## PLANAR HALL EFFECTS

The Planar Hall effect (PHE), initially observed in ferromagnetic materials, has a magnitude of only a few percent, resulting from the anisotropic magnetoresistance (AMR) induced by spin-orbit coupling. Subsequently, a giant magnitude PHE was found in devices made of (Ga, Mn)As [9], with four orders of magnitude larger than that observed in ferromagnetic metals. As interests in topological materials grow, PHE has been detected in a variety of newly identified topological insulators and Weyl semimetals. Theoretical studies [65–67] suggest a novel mechanism for PHE involving chiral anomaly and nontrivial Berry curvature, which are known to generate negative MR and in turn reinforce the PHE due to their enhancement of the AMR.

A common feature of materials that exhibit the PHE, especially in ferromagnetic materials, is the presence of a pronounced AMR. Consequently, planar Hall resistiv-

ity has been understood from the perspective of AMR. In this context, the electric field components ( $E_x, E_y$ ) and the current density  $J$  within the material's transport plane can be expressed as follows,

$$E_x = J\rho_{\perp} + J(\rho_{\parallel} - \rho_{\perp})\cos^2\theta \quad (6)$$

$$E_y = J(\rho_{\parallel} - \rho_{\perp})\sin\theta\cos\theta \quad (7)$$

where  $\rho_{\parallel}$  and  $\rho_{\perp}$  represent the resistivity when the current is parallel and perpendicular, respectively, to the magnetic field within the film plane. In other words the longitudinal resistivity  $\rho_{11}$  and the planar Hall resistivity  $\rho_{12}$  can be explicitly expressed as,

$$\rho_{11} = \rho_{\perp} - (\rho_{\perp} - \rho_{\parallel})\cos^2\theta \quad (8)$$

$$\rho_{12} = -(\rho_{\perp} - \rho_{\parallel})\sin\theta\cos\theta \quad (9)$$

where Eq. 8 describes the AMR, while Eq. 9 represents the planar Hall resistivity. To compare with the experimental results, we adopt the convention index for the resistivity elements, such that the  $x - y$  coordinate system is fixed with the sample ( $\rho_{11}, \rho_{12}$  refer to  $\rho_{xx}, \rho_{xy}$ ) and that the  $x' - y'$  coordinate system is rotated with magnetic field (the  $x'$  axis is parallel to the direction of magnetic field as  $\rho_{\parallel}, \rho_{\perp}$  refer to  $\rho_{x'x'}, \rho_{y'y'}$  respectively), which is shown in Fig.4 (j).

Meanwhile, PHE has also been observed in ordinary metals, such as bismuth. In 2020, a research group reported a significant PHE in bismuth, exceeding several  $\text{m}\Omega \cdot \text{cm}$  [68]. They utilized a semiclassical model with an adjustable tensor to simulate the multivalley and anisotropic Fermi surface of bismuth. This model effectively described the PHE behavior before reaching the quantum limit, where the magnetic field strength is not extremely high. Based on this work, another group confirmed the PHE in bismuth [69] and expanded the semiclassical model to include the quantum limit one by incorporating the charge carrier concentration approach to Landau quantization.

Contrasting with their manual adjustable model, we employ a tight-binding Hamiltonian derived from density functional theory calculations, without relying on any adjustable parameters. Remarkably, this approach enables us to reproduce all the distinctive features of the PHE of bismuth, with the exception of the quantum limit. Our calculations accurately depict the resistivity behavior across a range of moderate magnetic fields and temperatures. Fig.4(a)-(c) shows the experimental measurements, while Fig.4(d)-(f) displays our calculated resistivity results [70], demonstrating excellent agreement.

In Fig.4(d), the longitudinal resistivity  $\rho_{11}$  exhibits a periodic behavior, which is slightly deformed as magnetic field increases. For instance, at a very low magnetic field of  $B = 0.1 \text{ T}$ ,  $\rho_{11}$  shows four peaks of equal height and slight variations in the troughs, resembling a  $\frac{\pi}{2}$  period, although the exact period is  $\pi$ . As increasing magnetic

field, these four peaks at low fields transition into two m-shaped humps with central troughs. Additionally, in  $\rho_{22}$  (or  $\rho_{12}$ ), the peaks observed at  $\theta = \frac{\pi}{2}, \frac{3\pi}{2}$  (or  $\theta = \frac{\pi}{6}, \frac{7\pi}{6}$ ) at low fields evolve into valleys (part of valleys) with increasing magnetic field.

Similarly, the longitudinal resistivity  $\rho_{22}$  and the planar Hall resistivity  $\rho_{12}$  shown in Fig.4 (e) and (f) respectively, exhibit similar periodic tendencies as  $\rho_{11}$ . For the experimentally measured (Fig.4(c)) and our calculated (Fig.4(f)) planar Hall resistivity, at a low magnetic field of  $B\tau = 0.8 \text{ T}\cdot\text{ps}$ , the  $\rho_{12}$  curve (in blue) displays an approximate  $\frac{\pi}{2}$  period with distinct peaks and troughs. As the magnetic field increases, these peaks (or troughs) gradually flatten and disappear, eventually retaining only the troughs (or peaks) over a  $\frac{\pi}{2}$  range. This trend is clearly observable from  $B\tau = 1.6 \text{ T}\cdot\text{ps}$  to  $B\tau = 3.2 \text{ T}\cdot\text{ps}$ , corresponding to orange, green and red curves in Fig.4 (c) and (f).

The intricate period structure observed in the longitudinal  $\rho_{11}$ ,  $\rho_{22}$  and transverse resistivity  $\rho_{12}$  can be attributed to the interplay between symmetry and anisotropy of the Fermi surface geometry as the magnetic field rotates within the plane. It is also worth noting that the strength of the magnetic field plays a significant role in this interplay, thereby influencing the periodicity. For instance, in Fig.4 (g) and (h), when we examine the resistivity components  $\rho_{\parallel}$  and  $\rho_{\perp}$ , a six-fold symmetry becomes apparent. This symmetry arises because the projection of the Fermi surface onto the plane perpendicular to the current direction has  $C_3$  symmetry. Therefore, both  $\rho_{\parallel}$  and  $\rho_{\perp}$  exhibit this invariance, reflecting the six-fold symmetric nature of the Fermi surface geometry.

Before discussing the details of planar Hall resistivity, it is crucial to highlight the difference in AMR between ferromagnetic materials and bismuth when applying the rotation transformation, a detail that can be easily overlooked. To illustrate this point, we assume that the rotation transformation of Eq. 9 is correct to calculate the PHE of bismuth. With defining the longitudinal and transverse directions as the parallel and perpendicular axes respectively, we insert  $\rho_{\parallel}$  and  $\rho_{\perp}$  into  $\tilde{\rho}_{12}$  defined as  $\tilde{\rho}_{12} \equiv -(\rho_{\perp} - \rho_{\parallel})\sin\theta\cos\theta$  [71]. After plotting  $\tilde{\rho}_{12}$  in Fig.4 (i), however, it does not yield the same results as our direct calculations shown in Fig.4(f), which accurately replicate the experimental measurements in Fig.4 (c). The discrepancy arises because the traditional rotation transformation in Eq.9, commonly used for ferromagnetic materials, considers only the diagonal elements of the resistivity tensor, while completely overlooking the off-diagonal elements.

Therefore, it becomes essential to incorporate a rotation transformation that involves all elements of the resistivity tensor, especially for materials with a highly anisotropic Fermi surface, as follows (see detailed derivation in [59]),

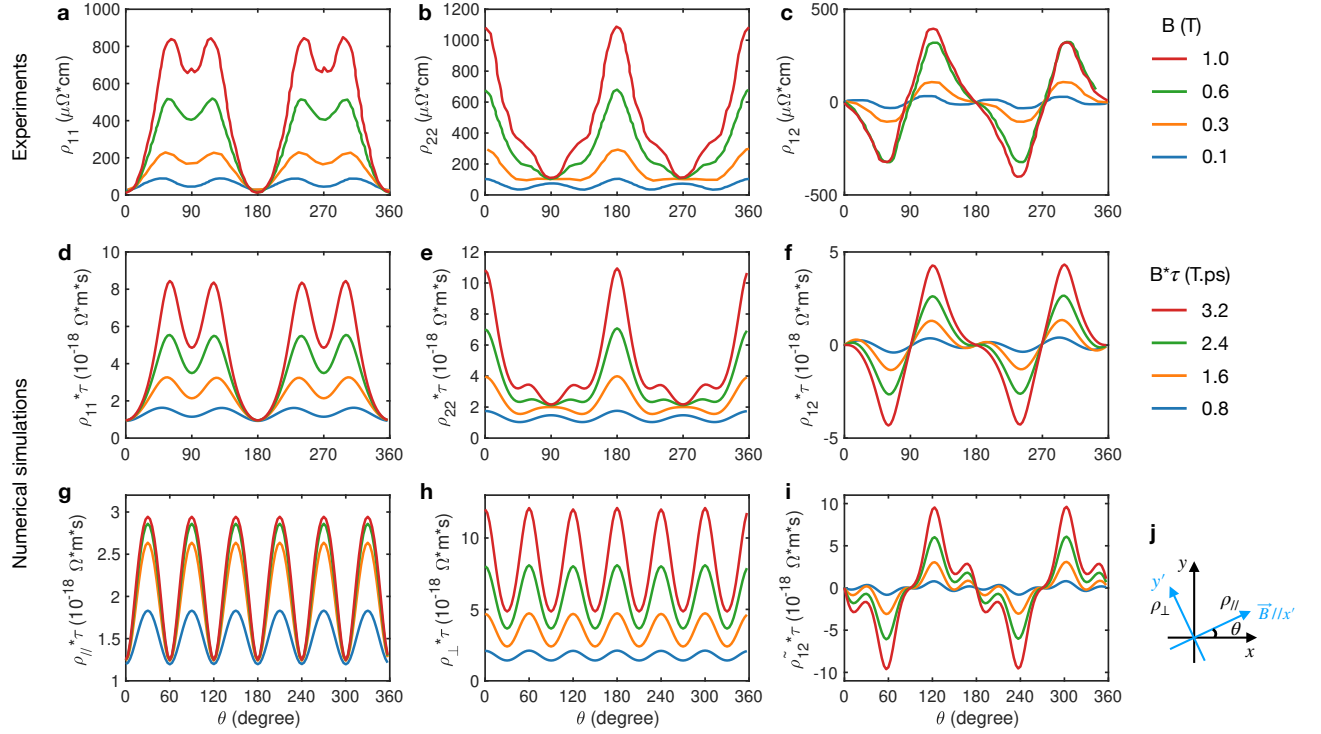


FIG. 4: Experimental and numerically simulated AMR and PHE curves of bismuth. (a-c) Experimentally observed angular dependence of (a)  $\rho_{11}$ , (b)  $\rho_{22}$  and (c)  $\rho_{12}$  (PHE) with the current along the binary axis, replotted from Ref. [68]. (d-f) Numerical simulations of AMR and PHE corresponding to (a-c). (g-h) Representations of AMR where (g)  $\rho_{\perp}$  and (h)  $\rho_{\parallel}$  represent the resistivity with the magnetic field perpendicular ( $90^\circ$ ) and parallel ( $0^\circ$ ) to the electric current. (i) Numerically simulated PHE calculated based on (g) and (h) (see Eqn. 8 and 9), excluding the off-diagonal contribution from the z-direction. (j) Schematic diagram of the rotation transformation coordinate.

$$\begin{pmatrix} \frac{1}{2}[\rho_{\parallel} + \rho_{\perp} + (\rho_{\parallel} - \rho_{\perp}) \cos 2\theta - (\rho_{x'y'} + \rho_{y'x'}) \sin 2\theta] & \frac{1}{2}[\rho_{x'y'} - \rho_{y'x'} + (\rho_{x'y'} + \rho_{y'x'}) \cos 2\theta + (\rho_{\parallel} - \rho_{\perp}) \sin 2\theta] & \rho_{x'z'} \cos \theta - \rho_{y'z'} \sin \theta \\ \frac{1}{2}[-\rho_{x'y'} + \rho_{y'x'} + (\rho_{x'y'} + \rho_{y'x'}) \cos 2\theta + (\rho_{\parallel} - \rho_{\perp}) \sin 2\theta] & \frac{1}{2}[\rho_{\parallel} + \rho_{\perp} + (-\rho_{\parallel} + \rho_{\perp}) \cos 2\theta - (\rho_{x'y'} + \rho_{y'x'}) \sin 2\theta] & \rho_{y'z'} \cos \theta + \rho_{x'z'} \sin \theta \\ \rho_{z'x'} \cos \theta - \rho_{z'y'} \sin \theta & \rho_{z'y'} \cos \theta + \rho_{z'x'} \sin \theta & \rho_{z'z'} \end{pmatrix} \quad (10)$$

The difference in the rotation transformation between Eq.9 and Eq.10 stems from the distinct AMR origins in ferromagnetic materials and bismuth. In ferromagnetic materials, an easy magnetization axis aligns with the external magnetic field, leading to significantly larger diagonal elements compared to off-diagonal elements in the resistivity tensor. Therefore, it is justified to use Eq.8 and Eq.9 for the rotation transformation, disregarding the off-diagonal resistivity elements in these materials. In contrast, due to bismuth's highly anisotropic Fermi surface, both diagonal ( $\rho_{\parallel}$ ,  $\rho_{\perp}$ ) and off-diagonal resistivity elements (in Eq. 10) are comparably significant. Consequently, a full rotation transformation is necessary to accurately replicate results, as illustrated in Fig.4(f) and (i).

With the full rotation of the resistivity tensor as shown in 10, we can gain a deeper understanding of the fine period structure, we examine the individual terms con-

tributing to the resistivity element  $\rho_{11}$ , which is expressed as  $\rho_{11} = \frac{1}{2}[(\rho_{\parallel} + \rho_{\perp}) + (\rho_{\parallel} - \rho_{\perp}) \cos 2\theta - (\rho_{x'y'} + \rho_{y'x'}) \sin 2\theta]$ . By analyzing these terms one by one, one observes the following features. At low magnetic field ( $B = 0.1$ T), the third term, involving  $(\rho_{x'y'} + \rho_{y'x'}) \sin 2\theta$ , displays a period of  $\frac{\pi}{2}$ , as shown in Fig.S1 [59]. This term predominantly influences the behavior of  $\rho_{11}$  in the low magnetic field regime. Conversely, at high magnetic field ( $B = 1$ T), the first and second terms, containing  $\rho_{\parallel}$  and  $\rho_{\perp}$ , which are nearly identical as demonstrated in Fig.S1 [59], become the principal contributors to  $\rho_{11}$ . The distinction in resistivity behavior under different magnetic field limits is quite logical, given that  $\rho_{\parallel}$  and  $\rho_{\perp}$  vary quadratically with the magnetic field (as  $B^2$ ), while  $\rho_{xy}$  and  $\rho_{yx}$  change linearly with  $B$ . As a result, at lower magnetic field, the third term comprising  $\rho_{xy}$  and  $\rho_{yx}$  predominantly influences the period structure. Conversely, at higher magnetic field, the first and second

terms, associated with  $\rho_{\parallel}$  and  $\rho_{\perp}$  respectively, become the key determinants.

In conclusion, the PHE is not a transport phenomenon exclusive to ferromagnetic and nontrivial topological materials; it also occurs in ordinary materials, such as bismuth. While the PHE in both ferromagnetic materials and bismuth arises from AMR, their underlying causes differ. In ferromagnetic materials, the PHE is mainly attributed to spin-orbit coupling. Whereas in bismuth, it results from the anisotropic Fermi surface geometry. This distinction necessitates a rigorous approach when applying rotation transformation to bismuth, requiring the inclusion of all resistivity tensor elements, not just the diagonal ones, as is typically done for ferromagnetic materials. In all, understanding the varying origins and mechanisms of PHE across different materials not only sheds light on the multifaceted nature of this phenomenon but also enhances our overall grasp of the underlying physics in diverse material systems.

## DISCUSSION

Motivated by recent advancements in the study of various Hall effects in both topologically trivial and nontrivial materials, we have undertaken a systematic investigation of transverse resistivity such as Hall and planar Hall resistivity in order to achieve a comprehensive understanding of resistivity originating from Fermi surface geometry. We first employed multi-band toy models to investigate the ordinary Hall resistivity with unusual features. These models allowed us to understand the Hall resistivity of multiband materials like PtTe<sub>2</sub>, which is similar to the AHE in ferromagnetic metals. Then we found that the Hall resistivity of materials with multi-type charge carriers, like ZrSiS and PtTe<sub>2</sub>, can be calculated and extrapolated for a series of temperatures. Notably, we found that this scaling behavior with temperature is analogous to Kohler's rule, commonly associated with longitudinal resistivity. Further, we expanded our analysis to explain the Planar Hall resistivity of bismuth, in this semiclassical framework. To conclude, our semiclassical Boltzmann transport theory combined with first principles calculation has provided valuable insights into the origins of the Hall effect arising from Fermi surface geometry. These findings are instrumental in clarifying existing controversies and setting the direction for future research in this area.

## ACKNOWLEDGMENTS

We acknowledge the invaluable discussions with X. Dai. This work was supported by the National Key R&D Program of China (Grant No. 2023YFA1607400, 2022YFA1403800), the National Natural Science Founda-

tion of China (Grant No.12274436, 11925408, 11921004), the Science Center of the National Natural Science Foundation of China (Grant No. 12188101), and H.W. acknowledge support from the Informatization Plan of the Chinese Academy of Sciences (CASWX2021SF-0102).

---

\* Electronic address: [hmweng@iphy.ac.cn](mailto:hmweng@iphy.ac.cn)

† Electronic address: [quansheng.wu@iphy.ac.cn](mailto:quansheng.wu@iphy.ac.cn)

- [1] E. H. Hall, *American Journal of Mathematics* **2**, 287 (1879).
- [2] E. H. Hall, *Philos. Mag.* **12**, 157 (1881).
- [3] N. Nagaosa, J. Sinova, S. Onoda, A. H. MacDonald, and N. P. Ong, *Rev. Mod. Phys.* **82**, 1539 (2010).
- [4] K. v. Klitzing, G. Dorda, and M. Pepper, *Phys. Rev. Lett.* **45**, 494 (1980).
- [5] M. I. Dyakonov and V. I. Perel, *Sov. Phys. JETP Lett.* **13**, 467 (1971).
- [6] M. Dyakonov and V. Perel, *Physics Letters A* **35**, 459 (1971).
- [7] K. Hong and N. Giordano, *Phys. Rev. B* **51**, 9855 (1995).
- [8] H. Ohno, *Science* **281**, 951 (1998).
- [9] H. X. Tang, R. K. Kawakami, D. D. Awschalom, and M. L. Roukes, *Phys. Rev. Lett.* **90**, 107201 (2003).
- [10] Q. Li, D. E. Kharzeev, C. Zhang, Y. Huang, I. Pletikosić, A. Fedorov, R. Zhong, J. Schneeloch, G. Gu, and T. Valla, *Nature Physics* **12**, 550 (2016).
- [11] S. L. Adler, *Phys. Rev.* **177**, 2426 (1969).
- [12] J. S. Bell and R. Jackiw, *Il Nuovo Cimento A (1965-1970)* **60**, 47 (1969).
- [13] M.-C. Chang and Q. Niu, *Phys. Rev. B* **53**, 7010 (1996).
- [14] G. Sundaram and Q. Niu, *Phys. Rev. B* **59**, 14915 (1999).
- [15] B. Arno, M. Ali, K. Hiroyasu, N. Qian, and Z. Josef, *The Geometric Phase in Quantum Systems* (Springer, Berlin, 2003).
- [16] D. Xiao, M.-C. Chang, and Q. Niu, *Rev. Mod. Phys.* **82**, 1959 (2010).
- [17] A. K. Majumdar and L. Berger, *Phys. Rev. B* **7**, 4203 (1973).
- [18] R. Schad, P. Beliën, G. Verbanck, V. V. Moshchalkov, and Y. Bruynseraede, *Journal of Physics: Condensed Matter* **10**, 6643 (1998).
- [19] Y. Shiomi, Y. Onose, and Y. Tokura, *Phys. Rev. B* **79**, 100404 (2009).
- [20] M. Bowen, K.-J. Friedland, J. Herfort, H.-P. Schönherr, and K. H. Ploog, *Phys. Rev. B* **71**, 172401 (2005).
- [21] A. Fernández-Pacheco, J. M. De Teresa, J. Orna, L. Morellon, P. A. Algarabel, J. A. Pardo, M. R. Ibarra, C. Magen, and E. Snoeck, *Phys. Rev. B* **78**, 212402 (2008).
- [22] J. Xiong, S. K. Kushwaha, T. Liang, J. W. Krizan, M. Hirschberger, W. Wang, R. J. Cava, and N. P. Ong, *Science* **350**, 413 (2015).
- [23] Q. Li, D. E. Kharzeev, C. Zhang, Y. Huang, I. Pletikosić, A. Fedorov, R. Zhong, J. Schneeloch, G. Gu, and T. Valla, *Nature Physics* **12**, 550 (2016).
- [24] M. Hirschberger, S. Kushwaha, Z. Wang, Q. Gibson, S. Liang, C. Belvin, B. Bernevig, R. Cava, and N. Ong, *Nature Materials* **15**, 1161 (2016).
- [25] N. Kumar, S. N. Guin, C. Felser, and C. Shekhar, *Phys. Rev. B* **98**, 041103 (2018).

- [26] A. A. Taskin, H. F. Legg, F. Yang, S. Sasaki, Y. Kanai, K. Matsumoto, A. Rosch, and Y. Ando, *Nature Communications* **8**, 1340 (2017).
- [27] H. Li, H.-W. Wang, H. He, J. Wang, and S.-Q. Shen, *Phys. Rev. B* **97**, 201110 (2018).
- [28] P. Li, C. H. Zhang, J. W. Zhang, Y. Wen, and X. X. Zhang, *Phys. Rev. B* **98**, 121108 (2018).
- [29] P. Li, C. Zhang, Y. Wen, L. Cheng, G. Nichols, D. G. Cory, G.-X. Miao, and X.-X. Zhang, *Phys. Rev. B* **100**, 205128 (2019).
- [30] L. Zhou, B. C. Ye, H. B. Gan, J. Y. Tang, P. B. Chen, Z. Z. Du, Y. Tian, S. Z. Deng, G. P. Guo, H. Z. Lu, F. Liu, and H. T. He, *Phys. Rev. B* **99**, 155424 (2019).
- [31] N. Zhang, G. Zhao, L. Li, P. Wang, L. Xie, B. Cheng, H. Li, Z. Lin, C. Xi, J. Ke, M. Yang, J. He, Z. Sun, Z. Wang, Z. Zhang, and C. Zeng, *Proceedings of the National Academy of Sciences* **117**, 11337 (2020).
- [32] D. Huang, H. Nakamura, and H. Takagi, *Phys. Rev. Res.* **3**, 013268 (2021).
- [33] H. Wang, Y.-X. Huang, H. Liu, X. Feng, J. Zhu, W. Wu, C. Xiao, and S. A. Yang, "Theory of intrinsic in-plane hall effect," (2022), [arXiv:2211.05978 \[cond-mat.mes-hall\]](https://arxiv.org/abs/2211.05978).
- [34] J. Zhou, W. Zhang, Y.-C. Lin, J. Cao, Y. Zhou, W. Jiang, H. Du, B. Tang, J. Shi, B. Jiang, X. Cao, B. Lin, Q. Fu, C. Zhu, W. Guo, Y. Huang, Y. Yao, S. S. P. Parkin, J. Zhou, Y. Gao, Y. Wang, Y. Hou, Y. Yao, K. Suenaga, X. Wu, and Z. Liu, *Nature* **609**, 46 (2022).
- [35] M. Kohler, *Annalen der Physik* **424**, 211 (1938).
- [36] M. Kohler, *Naturwissenschaften* **36**, 186 (1949).
- [37] M. N. Ali, J. Xiong, S. Flynn, J. Tao, Q. D. Gibson, L. M. Schoop, T. Liang, N. Haldolaarachchige, M. Hirschberger, N. P. Ong, and R. J. Cava, *Nature* **514**, 205 (2014).
- [38] Y. L. Wang, L. R. Thoutam, Z. L. Xiao, J. Hu, S. Das, Z. Q. Mao, J. Wei, R. Divan, A. Luican-Mayer, G. W. Crabtree, and W. K. Kwok, *Phys. Rev. B* **92**, 180402 (2015).
- [39] F. Han, J. Xu, A. S. Botana, Z. L. Xiao, Y. L. Wang, W. G. Yang, D. Y. Chung, M. G. Kanatzidis, M. R. Norman, G. W. Crabtree, and W. K. Kwok, *Phys. Rev. B* **96**, 125112 (2017).
- [40] J. Du, Z. Lou, S. Zhang, Y. Zhou, B. Xu, Q. Chen, Y. Tang, S. Chen, H. Chen, Q. Zhu, H. Wang, J. Yang, Q. Wu, O. V. Yazyev, and M. Fang, *Phys. Rev. B* **97**, 245101 (2018).
- [41] O. Pavlosiuk, P. Swatek, D. Kaczorowski, and P. Wiśniewski, *Phys. Rev. B* **97**, 235132 (2018).
- [42] A. I. U. Saleheen, R. Chapai, L. Xing, R. Nepal, D. Gong, X. Gui, W. Xie, D. P. Young, E. W. Plummer, and R. Jin, *npj Quantum Materials* **5**, 53 (2020).
- [43] Q. Chen, Z. Lou, S. Zhang, B. Xu, Y. Zhou, H. Chen, S. Chen, J. Du, H. Wang, J. Yang, Q. Wu, O. V. Yazyev, and M. Fang, *Phys. Rev. B* **102**, 165133 (2020).
- [44] R. Chapai, D. A. Browne, D. E. Graf, J. F. DiTusa, and R. Jin, *Journal of Physics: Condensed Matter* **33**, 035601 (2020).
- [45] J. Xu, F. Han, T.-T. Wang, L. R. Thoutam, S. E. Pate, M. Li, X. Zhang, Y.-L. Wang, R. Fotovat, U. Welp, X. Zhou, W.-K. Kwok, D. Y. Chung, M. G. Kanatzidis, and Z.-L. Xiao, *Phys. Rev. X* **11**, 041029 (2021).
- [46] S. Zhang, Q. Wu, Y. Liu, and O. V. Yazyev, *Phys. Rev. B* **99**, 035142 (2019).
- [47] Y. Zhou, Z. Lou, S. Zhang, H. Chen, Q. Chen, B. Xu, J. Du, J. Yang, H. Wang, C. Xi, L. Pi, Q. Wu, O. V. Yazyev, and M. Fang, *Phys. Rev. B* **102**, 115145 (2020).
- [48] J. Du, Z. Lou, S. Zhang, Y. Zhou, B. Xu, Q. Chen, Y. Tang, S. Chen, H. Chen, Q. Zhu, H. Wang, J. Yang, Q. Wu, O. V. Yazyev, and M. Fang, *Phys. Rev. B* **97**, 245101 (2018).
- [49] Q. Chen, Z. Lou, S. Zhang, B. Xu, Y. Zhou, H. Chen, S. Chen, J. Du, H. Wang, J. Yang, Q. Wu, O. V. Yazyev, and M. Fang, *Phys. Rev. B* **102**, 165133 (2020).
- [50] G. Gatti, D. Gosálbez-Martínez, Q. S. Wu, J. Hu, S. N. Zhang, G. Autès, M. Puppini, D. Bugini, H. Berger, L. Moreschini, I. Vobornik, J. Fujii, J.-P. Ansermet, O. V. Yazyev, and A. Crepaldi, *Phys. Rev. B* **104**, 155122 (2021).
- [51] Q. Chen, Z. Lou, S. Zhang, Y. Zhou, B. Xu, H. Chen, S. Chen, J. Du, H. Wang, J. Yang, Q. Wu, O. V. Yazyev, and M. Fang, *Phys. Rev. B* **104**, 115104 (2021).
- [52] M. Novak, S. N. Zhang, F. Orbančić, N. Biliškov, G. Eguchi, S. Paschen, A. Kimura, X. X. Wang, T. Osada, K. Uchida, M. Sato, Q. S. Wu, O. V. Yazyev, and I. Kokanović, *Phys. Rev. B* **100**, 085137 (2019).
- [53] T. Liang, J. Lin, Q. Gibson, S. Kushwaha, M. Liu, W. Wang, H. Xiong, J. A. Sobota, M. Hashimoto, P. S. Kirchmann, Z.-X. Shen, R. J. Cava, and N. P. Ong, *Nature Physics* **14**, 451 (2018).
- [54] G. Kresse and J. Furthmüller, *Phys. Rev. B* **54**, 11169 (1996).
- [55] G. Kresse and D. Joubert, *Phys. Rev. B* **59**, 1758 (1999).
- [56] A. A. Mostofi, J. R. Yates, G. Pizzi, Y.-S. Lee, I. Souza, D. Vanderbilt, and N. Marzari, *Computer Physics Communications* **185**, 2309 (2014).
- [57] Y. Liu, H.-J. Zhang, and Y. Yao, *Phys. Rev. B* **79**, 245123 (2009).
- [58] Q. Wu, S. Zhang, H.-F. Song, M. Troyer, and A. A. Soluyanov, *Computer Physics Communications* **224**, 405 (2018).
- [59] [URL\\_will\\_be\\_inserted\\_by\\_publisher](#) (2023), supplementary materials.
- [60] E. Fawcett, *Advances in Physics* **13**, 139–191 (1964).
- [61] O. Pavlosiuk and D. Kaczorowski, *Scientific Reports* **8**, 11297 (2018).
- [62] A. Pippard, *Magnetoresistance in Metals* (Cambridge University Press, London, 1990).
- [63] R. Singha, A. K. Pariari, B. Satpati, and P. Mandal, *Proceedings of the National Academy of Sciences of the United States of America* **114**, 2468 (2017).
- [64] M. Ziman, *Electrons and Phonons* (Clarendon Press, Oxford, 1962).
- [65] A. A. Burkov, *Phys. Rev. B* **96**, 041110 (2017).
- [66] S. Nandy, G. Sharma, A. Taraphder, and S. Tewari, *Phys. Rev. Lett.* **119**, 176804 (2017).
- [67] Y.-W. Wei, J. Feng, and H. Weng, *Phys. Rev. B* **107**, 075131 (2023).
- [68] S.-Y. Yang, K. Chang, and S. S. P. Parkin, *Phys. Rev. Res.* **2**, 022029 (2020).
- [69] A. Yamada and Y. Fuseya, *Phys. Rev. B* **103**, 125148 (2021).
- [70] Here the resistivity elements  $\rho_{11}, \rho_{22}, \rho_{12}$ , shown in Fig.4(d)-(f), are calculated from Eq.10 rather than Eq.8 and Eq.9.
- [71] Here we use  $\tilde{\rho}_{12}$  (plotted in Fig.4(i)) to represent the planar Hall resistivity derived from the transformation of Eq.9. for bismuth, in order to distinguish it from the one( $\rho_{12}$ ) calculated using Eq.10 as shown in Fig.4(f).